

# Functionalization of graphene by intercalation: A theoretical insight

Vittoria Urso

Department of Physics, Sapienza Università di Roma, 00185 Rome, Italy; [vittoria.urso@uniroma1.it](mailto:vittoria.urso@uniroma1.it)

## CITATION

Urso V. Functionalization of graphene by intercalation: A theoretical insight. *Characterization and Application of Nanomaterials*. 2025; 8(2): 10326. <https://doi.org/10.24294/can10326>

## ARTICLE INFO

Received: 14 November 2024  
Accepted: 18 March 2025  
Available online: 6 May 2025

## COPYRIGHT



Copyright © 2025 Author(s).  
*Characterization and Application of Nanomaterials* is published by EnPress Publisher, LLC. This work is licensed under the Creative Commons Attribution (CC BY) license. <https://creativecommons.org/licenses/by/4.0/>

**Abstract:** The intercalation of alkali metals in graphene monolayers and bilayers has been studied using first-principles calculations in particular density functional theory. Alkali metals intercalate into graphite, leading to the formation of M-graphene layered materials (with M = Li, Na, K, Rb, and Cs). Intercalated species can modify the very electronic structure of graphene and consequently its electron mobility. Thanks to various experimental studies, it has been possible to demonstrate that alkali metal intercalation can be used to modify the electronic structure close to the Fermi level of the M-graphene materials and manipulate the carrier mobility and therefore we want to do this also with computational studies. These materials have a wide variety of applications, especially for the development of new batteries and other devices. The first principles are discussed on the effects of the intercalation of a heavy-alkali metal (K) on the electronic structure of graphene monolayers and bilayers.

**Keywords:** graphene; alkali metals; intercalation; Dirac cone shift

**PACS numbers:** 71.10.-w; 78.20.Bh; 81.05.ue

## 1. Introduction

Graphene is the most studied of two-dimensional (2D) materials [1–6], pristine free-standing graphene has a high electron mobility, which is reduced when deposited on a substrate due to graphene-substrate interactions [7–12]. Graphene and carbon nanotube CNTs are among the most prominent nanoscale materials currently studied [13]. Two-dimensional (2D) graphene [14] has a rather unique sublattice symmetry and is a zero-gap semiconductor with a point-like Fermi surface and a linear dispersion at the Fermi level; these properties are responsible for observed ballistic transport, Dirac-type quasiparticles, and anomalous quantum Hall effects [15]. Graphene is a flat monolayer of carbon atoms tightly packed in a two-dimensional (2-D) honeycomb lattice and is a basic building block for graphitic materials of all other dimensions [16] as shown in **Figure 1**.

Its interesting electrical and transport properties have attracted much attention since its discovery in 2004. Graphene is one atom thick and its very high mobility allows the quantum Hall effects to be observed even at room temperature [17]. Alkali metals adsorbed on metallic substrates have been studied for a long time [18,19], but the nature of the alkali-substrate bond is not yet fully understood. A subset of these studies concerns the adsorption of alkali in graphite [19]. The electronic properties of graphite can change dramatically due to intercalators; for example, electrical conductivity along the planes increases dramatically [19]. Potassium (K) has been the most studied of all alkali metals intercalated on graphite [20–24]. The first step in studying the surface structure of K in graphite is the intercalation process [25]. In **Figure 2** there are some

methods of intercalation of K on graphite, in particular methods for investigating the coverage of K/graphite, in the last column you can find a reference for each experiment:

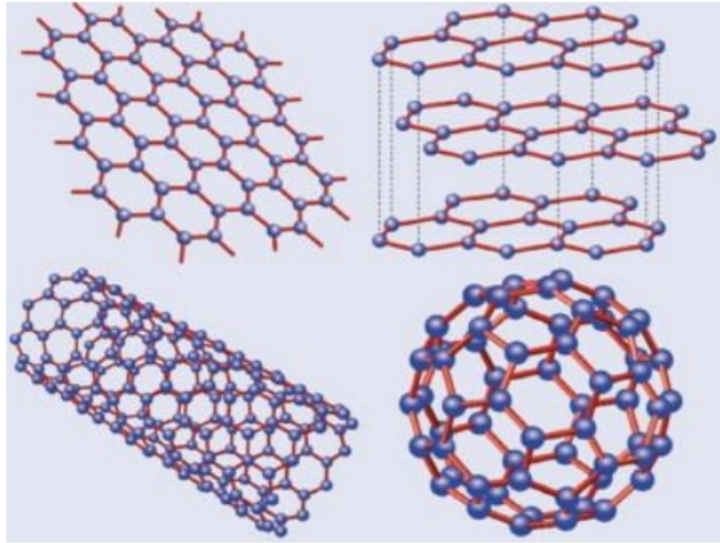


**Figure 1.** Carbon allotropes. Top left: Graphene 2-D; top right: Graphite 3-D; bottom left: nanotube 1-D; bottom right: fullerene 0-D [17].

$\theta_c$	T (K)	Method	Signature	References
0.1	90	LEED	Diffraction ring stops moving and (2 x 2) appears	[18]
0.1	90	EELS	Plasmon mode stops shifting	[18]
0.35	85	Work function	Kink in $\phi$ versus $\theta$	[5]
0.30	85	HREELS	I max of 17 meV peak	[5]
0.25	85	LEED	Appearance of (2 x 2) structure	[5]
0.3-0.4	160	UPS	Appearance of K band	[5]
0.30	90	PD exp.	Max PD yield	[28]
0.12	90	HR-LEED	Appearance of (2 x 2) structure	[10]
>0.25	??	Ab initio slab calc.	'Ionic-like' charge density profile	[29]
0.25	90	HREELS	Leveling of surface plasmon energy	[30]

**Figure 2.** Critical coverage for K/graphite condensation taken from reference [25].

## 2. Theory

Graphene is made out of carbon atoms with a structure shown in **Figure 3** [26]. The lattice vectors can be written as

$$\mathbf{a}_1 = \frac{a}{2}(3, \sqrt{3}) \quad \mathbf{a}_2 = \frac{a}{2}(3, -\sqrt{3}) \quad (1)$$

where  $a \approx 1.42\text{\AA}$ . The reciprocal-lattice vectors are given by

$$\mathbf{b}_1 = \frac{2\pi}{3a}(1, \sqrt{3}) \quad \mathbf{b}_2 = \frac{2\pi}{3a}(1, -\sqrt{3}). \quad (2)$$

The two points  $K$  and  $K'$  at the corners of the Brillouin zone (BZ) are of particular importance, these are named Dirac points, their positions in momentum space are [26]:

$$\mathbf{K} = \left( \frac{2\pi}{3a}, \frac{2\pi}{3\sqrt{3}a} \right) \quad \mathbf{K}' = \left( \frac{2\pi}{3a}, -\frac{2\pi}{3\sqrt{3}a} \right). \quad (3)$$

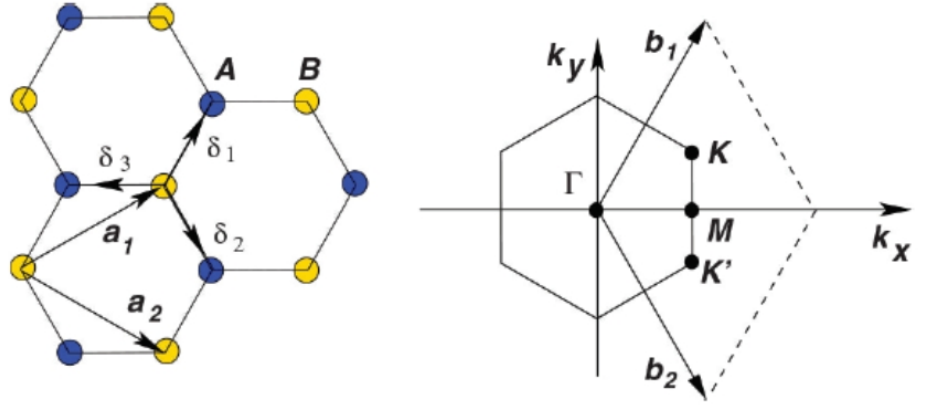


**Figure 3.** Honeycomb lattice and its Brillouin zone. Left: lattice structure of graphene, made out of two interpenetrating triangular lattices ( $\mathbf{a}_1$  and  $\mathbf{a}_2$  are the lattice unit vectors, and  $\delta_i$ ,  $i = 1, 2, 3$  are the nearest-neighbor vectors). Right: corresponding Brillouin zone. The Dirac cones are located at the  $K$  and  $K'$  points [26].

The three nearest-neighbor vectors in real space are given by

$$\delta_1 = \frac{a}{2}(1, \sqrt{3}), \quad \delta_2 = \frac{a}{2}(1, -\sqrt{3}), \quad \delta_3 = -a(1, 0). \quad (4)$$

Usually the Schrödinger equation is quite sufficient to describe the electronic properties of materials. Charge carriers in semiconductors have a non-zero effective mass and their behavior can be well described by Schrödinger's equation. Graphene is an exception [27–30]: its charge carriers behave like relativistic particles and therefore it is more natural to describe them with the Dirac equation rather than the Schrödinger equation [31] (see **Figure 4**).

The tight-binding Hamiltonian for electrons is:

$$H = -t \sum_{\langle i,j \rangle, \sigma} (a_{\sigma,i}^+ b_{\sigma,j} + H.c.) - t' \sum_{\langle\langle i,j \rangle\rangle, \sigma} (a_{\sigma,i}^+ a_{\sigma,j} + b_{\sigma,i}^+ b_{\sigma,j} + H.c.) \quad (5)$$

where  $t \approx 2.8$  eV is the nearest-neighbor hopping energy and  $t' = 0.1$  eV (obtained from ab initio calculations) is the next nearest-neighbor hopping energy. The energy bands have the form:

$$E_{\pm}(\mathbf{k}) = \pm t \sqrt{3 + f(\mathbf{k})} - t' f(\mathbf{k}) \quad (6)$$

with

$$f(\mathbf{k}) = 2 \cos(\sqrt{3}k_y a) + 4 \cos\left(\frac{\sqrt{3}}{2}k_y a\right) \cos\left(\frac{3}{2}k_x a\right) \quad (7)$$

where the plus sign applies to the upper ( $\pi^*$ ) and the minus sign to the lower ( $\pi$ ) band, from Equation (7) can be seen that the spectrum is symmetric around zero energy if  $t' = 0$ . For a finite value of  $t'$ , the electron-hole symmetry is broken and the  $\pi$  and  $\pi^*$  bands become asymmetric. In **Figure 5** there is the full band structure with both  $t$  and  $t'$ , there is also a zoom in of the band structure close to one of the Dirac points (at the  $K$  or  $K'$  point in the BZ). This dispersion can be obtained by expanding the full band structure, Equation (7), close to the  $\mathbf{K}$  (or  $\mathbf{K}'$ ) vector, Equation (3), as  $\mathbf{k} = \mathbf{K} + \mathbf{q}$ , with  $|\mathbf{q}| \ll |\mathbf{K}|$

$$E_{\pm}(\mathbf{q}) \approx \pm v_F |\mathbf{q}| + O[(q/K)^2] \quad (8)$$

where  $v_F$  is the Fermi velocity, given by  $v_F = 3ta/2$ , with a value of  $v_F \simeq 1 \times 10^6$  m/s. The most important difference between this result and the usual case  $\epsilon(\mathbf{q}) = q^2/(2m)$ , where  $m$  is the electron mass, is that the Fermi velocity does not depend on the energy or momentum.

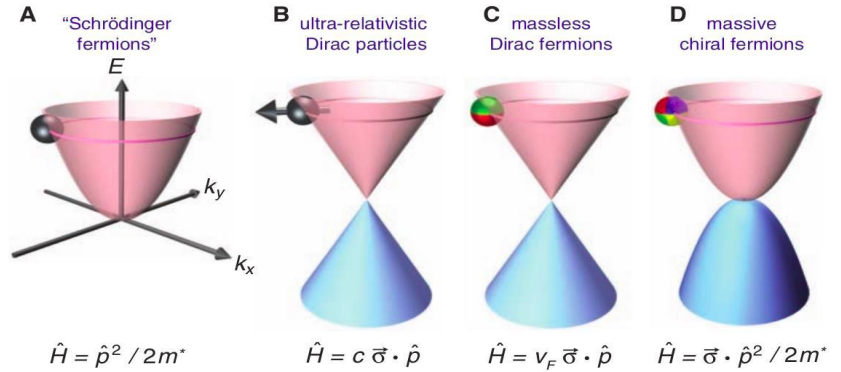


**Figure 4.** (A) Charge carriers are normally described by the Schrödinger equation with an effective mass  $m^*$  different from the free electron mass ( $p$  is the momentum operator). (B) Relativistic particles in the limit of zero rest mass follow the Dirac equation, where  $c$  is the speed of light and  $\sigma$  is the Pauli matrix. (C) Charge carriers in graphene are called massless Dirac fermions, with the Fermi velocity  $v_F = 1 \times 10^6$  m/s playing the role of the speed of light. (D) Bilayer graphene provides us another type of quasi-particles: they are massive Dirac fermions described by a rather bizarre Hamiltonian that combines features of both Dirac and Schrödinger equations [31].

The coverage-dependent behavior of K/graphite is obtained by means of a combination of one-dimensional low energy electron diffraction (LEED) and electron energy loss spectroscopy (EELS): low covers can be prepared in which the K atoms are partially ionized and evenly distributed over the surface due to dipole-dipole interactions. As coverage increases, the upper layer compresses uniformly until it reaches a critical coverage ( $\Theta$ ) of 0.1 monolayer (ML) [19]. Coverages below this limit are defined as dispersed phase, while the critical coverage (0.1 ML) will be referred to as saturated dispersed phase. At 0.1 ML, potassium forms approximately a covering layer ( $7 \times 7$ ). Above 0.1 ML, islands ( $2 \times 2$ ) start to nucleate until the covering layer

$(2 \times 2)$  is fully developed and corresponds to  $\Theta = 1$  ML. The region between 0.1 and 1 ML will be defined as mixed phase.

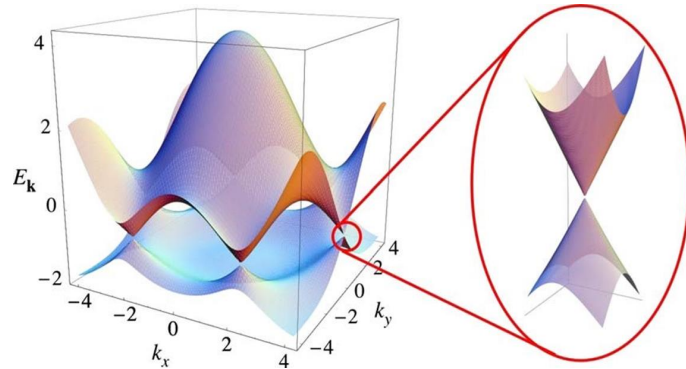


**Figure 5.** Electronic dispersion in the honeycomb lattice. Left: energy spectrum. Right: zoom in of the energy bands close to one of the Dirac points.

### 3. Computational details

Calculations are performed within the first-principles density functional theory (DFT) under the local density approximation (LDA). Our main goal is to observe the effect of doping on graphene, and since we are not directly interested in describing long-range interactions or structural distortions, we focus on the simplest approach: LDA. LDA is sufficient to observe charge transfer from the alkali metal to graphene, changes in the electronic bands of graphene, such as filling of conduction bands, and changes in local electronic properties, such as the change of the density of states (DOS) near the Fermi level. LDA is an approximation that works well when dispersion effects (van der Waals forces) are not dominant or are not crucial for the interaction between the alkali metal and graphene; there are no large structural distortions in the graphene lattice that significantly affect the geometry or symmetry of the electronic bands. LDA is preferred in all cases like these for computational simplicity because it is less computationally expensive than GGA making it more suitable for preliminary studies or large-scale simulations and for the description of local electronic changes; and because LDA can provide an accurate idea of the change in electron density and energy levels as a result of doping without the need to deal with the weak interactions between the alkali metal and graphene. In practice we use the so-called “rigid band model”, a simple model in which the interaction between graphite and an adsorbate or intercalant is limited to the donation or removal of the charge by the atom, with no other influences on the graphite bands [19]. The model thus allows us to understand the observed binding energy shifts, estimate the amount of charge transferred, etc. The QUANTUM ESPRESSO package is used to perform all calculations [32]. The primitive unit cell and the experimental value of the lattice constant are shown in **Figure 6**, my calculated lattice constant is  $2.44 \text{ \AA} = \sqrt{3} \times 1.41 \text{ \AA}$ , which is slightly smaller than the experimental value.

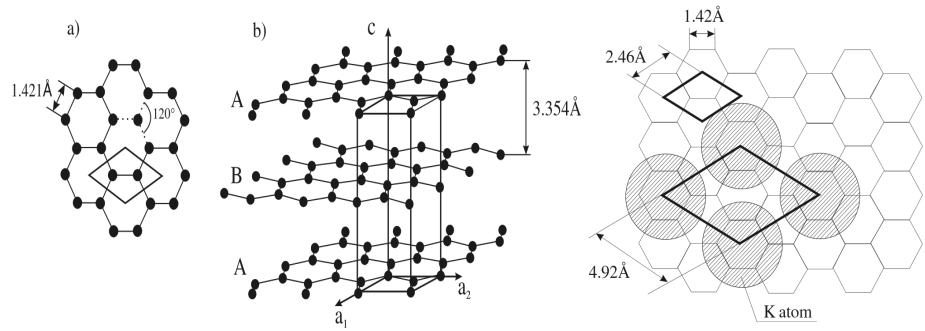


**Figure 6.** On the left: Model of (a) two-dimensional and (b) three-dimensional graphite together with the structural parameters. In (a), the surface unit cell, containing two C atoms, is highlighted. On the right: A schematic diagram of the  $(2 \times 2)$  structure formed by K on the graphite surface. Both the substrate and the overlayer unit cells are represented [25].

Calculations for the isolated graphene layer  $(2 \times 2)$  and  $(4 \times 4)$ , the isolated adatom layer  $(2 \times 2)$  and  $(4 \times 4)$ , and the adatom-graphene system  $(2 \times 2)$  and  $(4 \times 4)$  are performed with the same hexagonal supercell. The Brillouin zone is sampled with a grid of  $8 \times 8 \times 1$   $k$  points centered on  $\Gamma$ , and Gaussian smearing with a width of  $\sigma = 0.01$  eV is used for the occupation of the electronic levels. A larger supercell improves the description of the interactions between alkalines and graphene, reducing periodic confinement effects and improving the convergence of physical properties. Finer sampling of the Brillouin zone allows for a better description of electronic bands and densities of states, especially in regions close to the Dirac points of graphene. With alkaline intercalation, the effect on electronic bands (e.g., shifting of conduction bands or formation of new states) can be more precisely predicted. The self-consistency convergence threshold was set at  $1.0d - 9$ , the convergence threshold on total energy at  $1.0d - 5$ , and the convergence threshold on forces (a.u.) at  $1.0d - 4$ . We have performed calculations of K on graphite at the H site; see **Figure 7**:

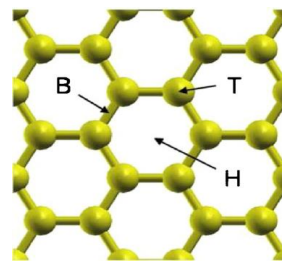


**Figure 7.** The three adsorption sites: Hollow H, bridge B, and top T [33].

## 4. Results

We have analyzed 11 different systems through self-consistent field calculations with QUANTUM ESPRESSO under the local density approximation (LDA) and Perdew-Zunger functionals and the Von Barth-Car method (pz-vbc), including spin polarization, and we have obtained the results showed in **Table 1**:

**Table 1.** The results of all systems, the greater the shift of the Dirac cone the greater the doping.

System	Total energy (eV) /num. atoms	Schift Dirac cone (eV)	$d_{k-graphene}$ (Å)
1. $KC_8$	-138.9405	-1.07	2.89
2. $KC_{32}$	-150.6698	-0.90	2.73
2bis. $KC_{32}$ (s = 2)	-150.6703	-0.88	2.73
3. $K_4C_{32}$	-138.9397	-1.07	2.93
4. $K_4C_{32}$ (alt. side)	-138.9153	-1.18	2.84
5. $K_4C_{32}$ (check.)	-138.9153	-1.18	2.83
6. $C_8KC_8$ (st. AB)	-146.5524	-1.07	2.84
7. $C_8KC_8$ (st. AA)	-146.5547	-1.18	2.85
8. $KC_8C_8$	-146.54465	-1.07	2.91
9. $KC_8C_8K$	-138.9507	-1.07	2.92
10. $KC_2$	-105.6311	-2.30	2.66
11. $K_2C_{32}$	-146.5225	-0.98	2.83

The following subsections show the systems visualized with xcrsden and the DOS visualized with xmgrace.

#### 4.1. $KC_8$

In **Figure 8** the  $KC_8$  system is shown and in **Figure 9** its DOS.

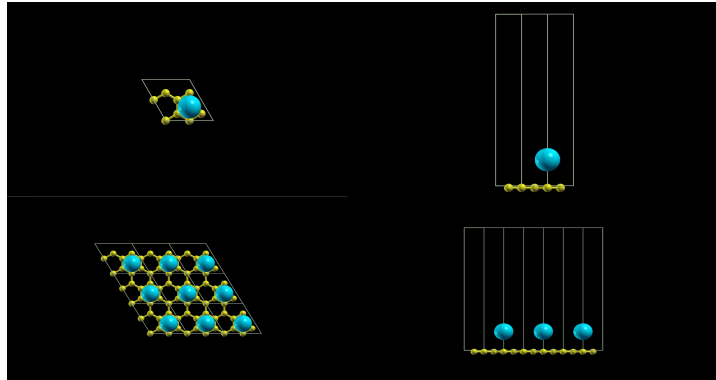


**Figure 8.** In the upper there is the  $KC_8$  system in top view (on the left) and in side view (on the right) in  $(2 \times 2)$  unit cell and in the lower there is the replicated  $KC_8$  system in the top view (on the left) and in the side view (on the right) in  $(6 \times 6)$  unit cell. The carbon-carbon distance is  $d_{c-c} = 1.4106 \text{ \AA}$ .

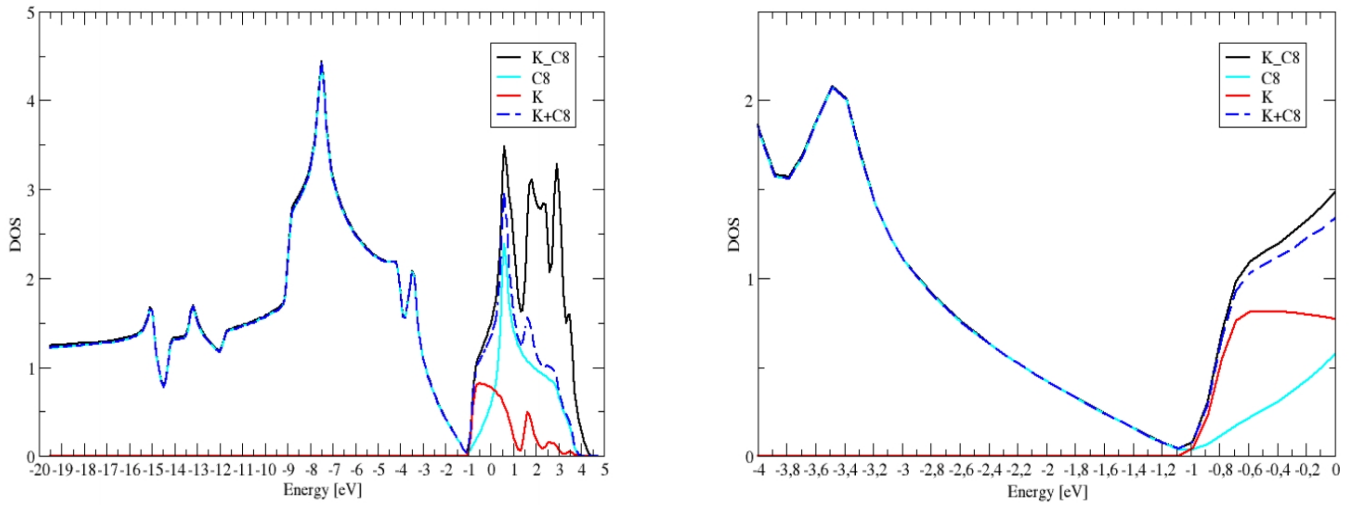


**Figure 9.** The DOS (density of states) of the  $KC_8$  system, on the left the full DOS and on the right a range of energy around the Fermi level.

In **Figure 10** are shown the PDOS (projected DOS).

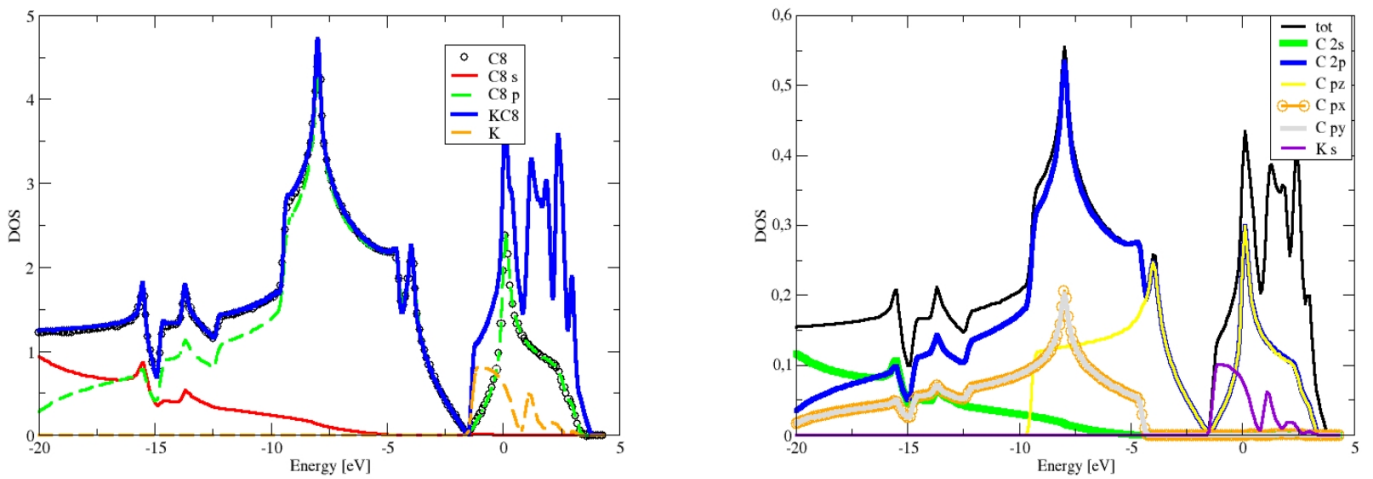


**Figure 10.** The full and its partial DOS  $s$  and  $p$ .

#### 4.2. $KC_{32}$

In **Figure 11** the  $KC_{32}$  system is shown and in **Figure 12** its DOS.

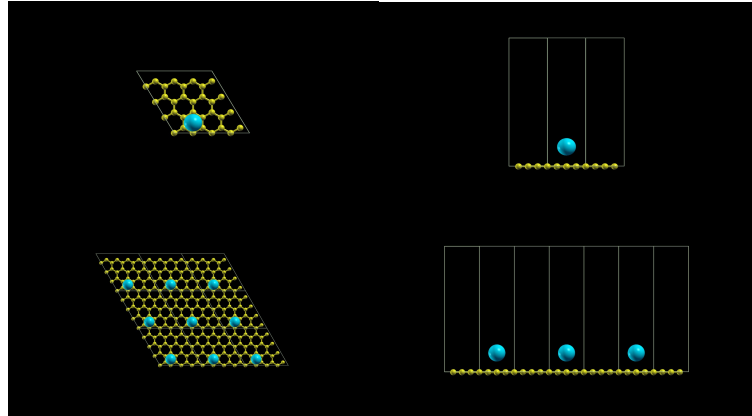


**Figure 11.** In the upper there is the  $KC_{32}$  system in top view (on the left) and in side view (on the right) in  $(4 \times 4)$  unit cell and in the lower there is the replicated  $KC_{32}$  system in the top view (on the left) and in the side view (on the right) in  $(12 \times 12)$  unit cell. The carbon-carbon distance is  $d_{c-c} = 1.4106$ .

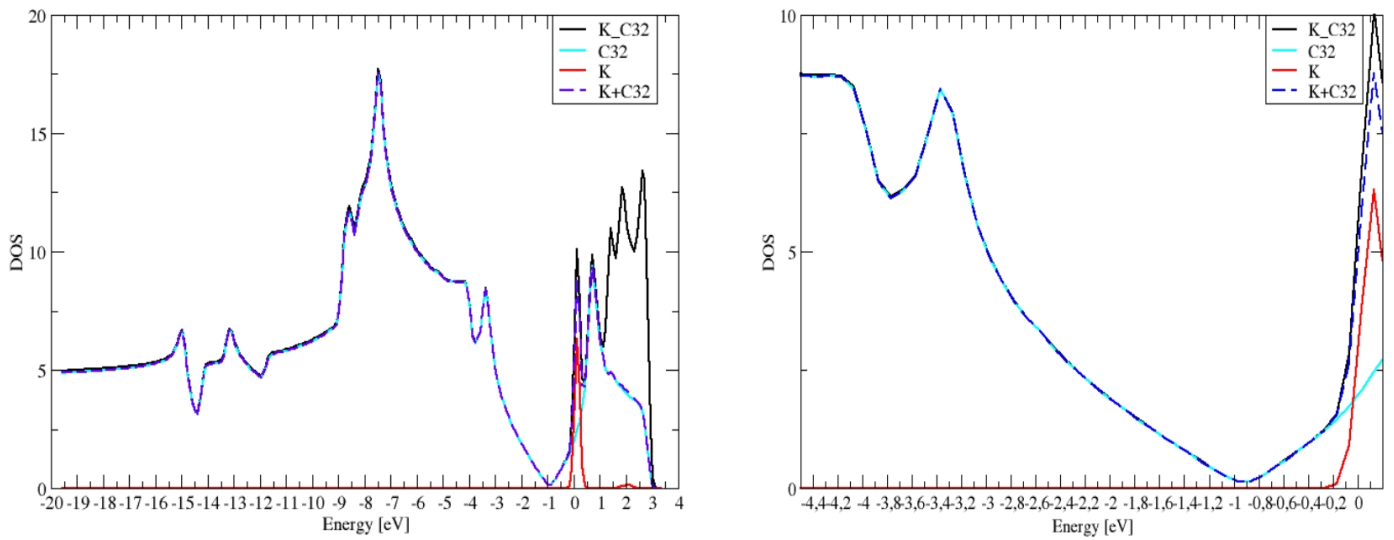


**Figure 12.** The DOS of the  $KC_{32}$  system, on the left the full DOS and on the right a range of energy around the Fermi level.

Only in this case do we have a magnetic case as shown in **Figures 13** and **14**.

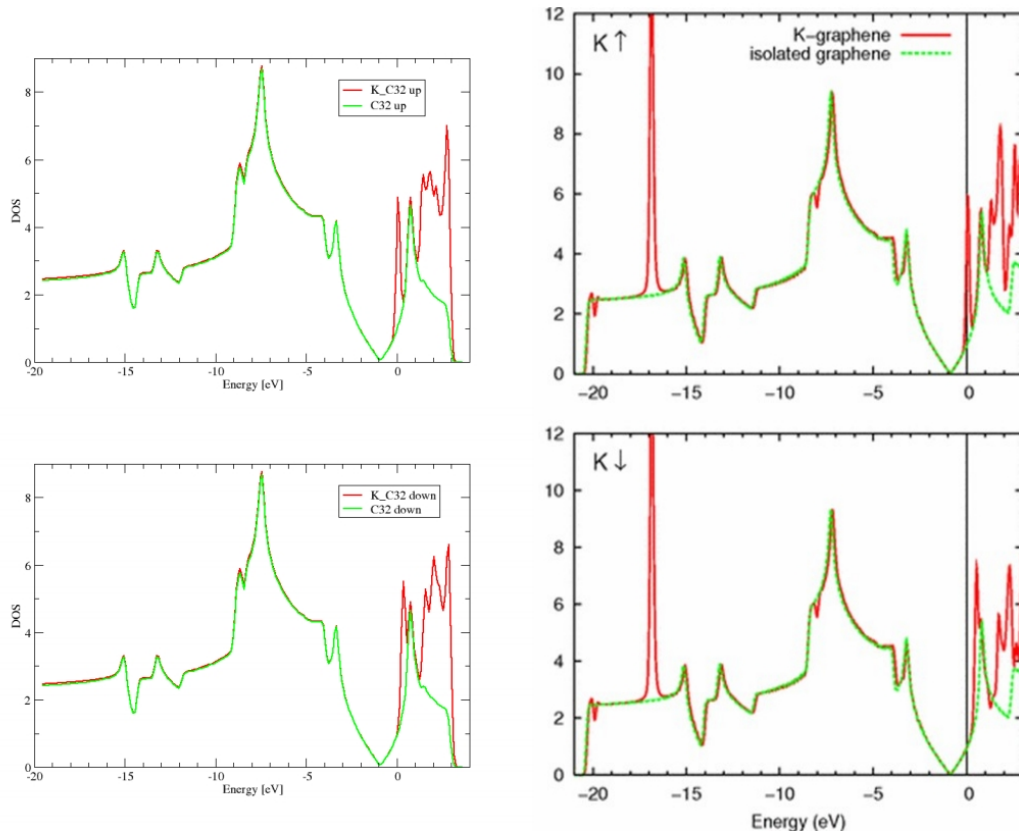


**Figure 13.** The DOS of the  $KC_{32}$  system with spin = 2, on the left the DOS of my calculation and on the right the DOS of **Figure 3** of the reference [34].

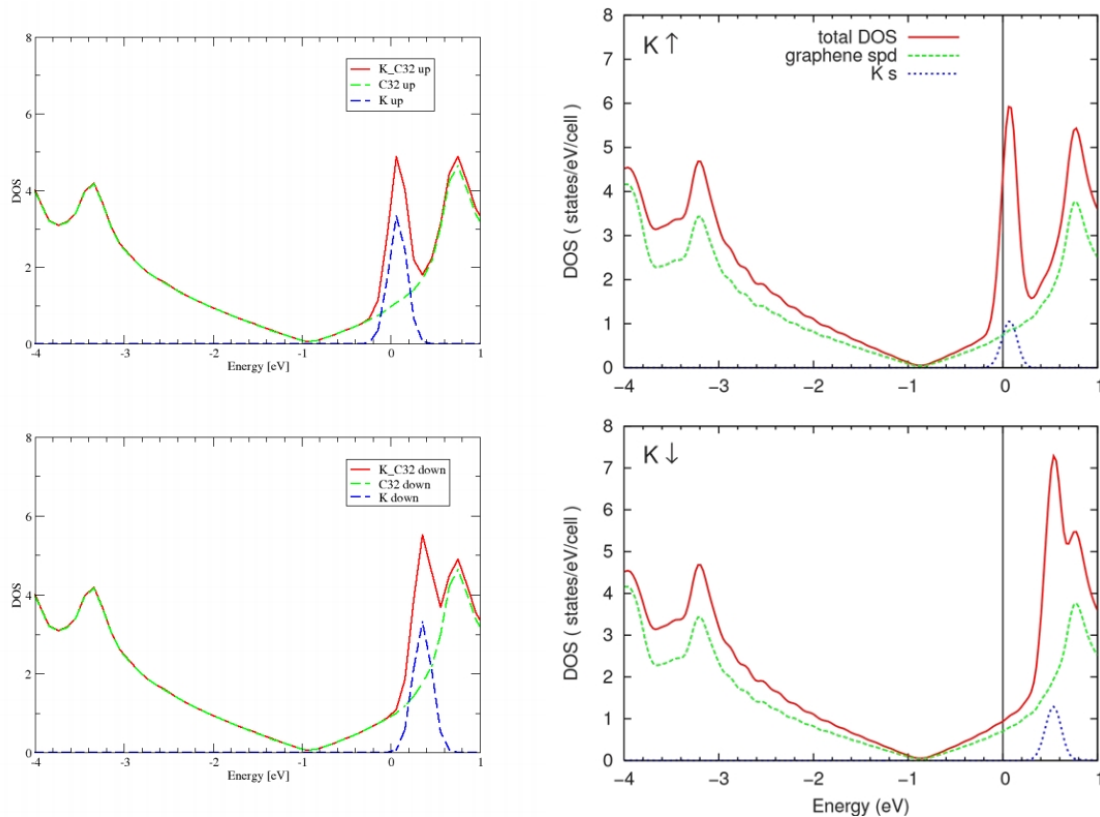


**Figure 14.** The DOS of the  $KC_{32}$  system with spin = 2, on the left a range of energy around the Fermi level of my DOS and on the right **Figure 4** of the reference [34].

### 4.3. $K_4C_{32}$

In **Figure 15** the  $K_4C_{32}$  system is shown and in **Figure 16** its DOS.

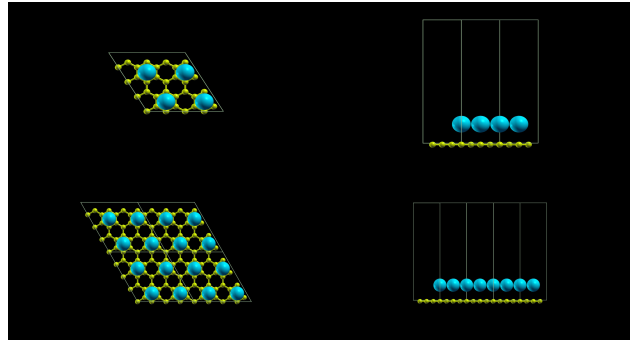


**Figure 15.** In the upper there is the  $K_4C_{32}$  with  $(4 \times 4)$  cell and in the lower there is the replicated  $K_4C_{32}$  system. The carbon-carbon distance is  $d_{c-c} = 1.4102$ .

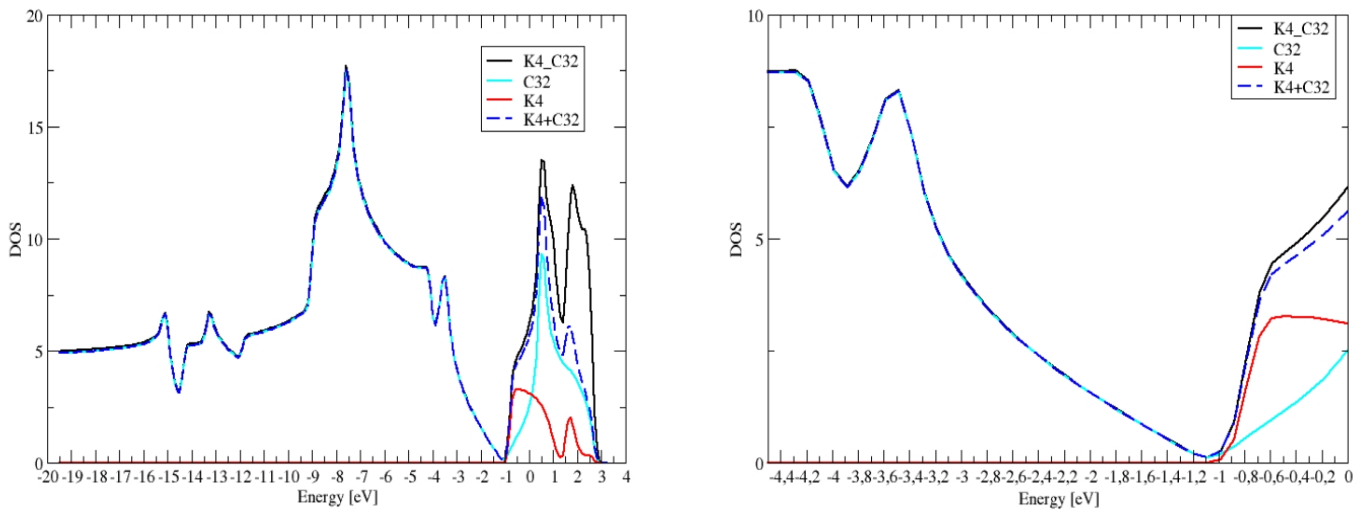


**Figure 16.** The DOS of the  $K_4C_{32}$  system, on the left the full DOS and on the right a range of energy around the Fermi level.

### 4.4. $K_4C_{32}$ with K on alternate side

In **Figure 17** the  $K_4C_{32}$  with K on alternate side system is shown and in **Figure 18** its DOS.

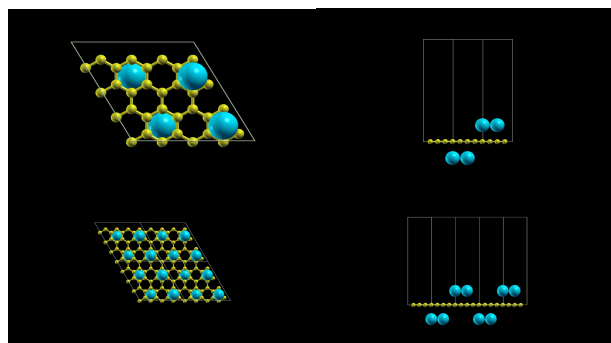


**Figure 17.** In the upper there is the  $K_4C_{32}$  system with  $(4 \times 4)$  cell and in the lower there is the replicated  $K_4C_{32}$  system. The carbon-carbon distance is  $d_{c-c} = 1.4119$ .

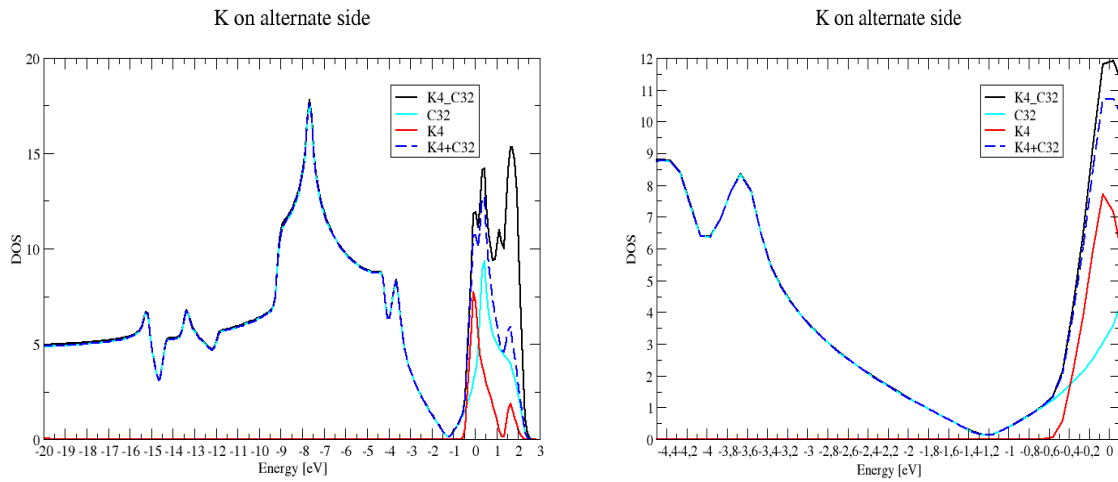


**Figure 18.** The DOS of the  $K_4C_{32}$  system, on the left the full DOS and on the right a range of energy around the Fermi level.

#### 4.5. $K_4C_{32}$ with K at checkerboard

In **Figure 19** the  $K_4C_{32}$  with K at checkerboard system is shown and in **Figure 20** its DOS.

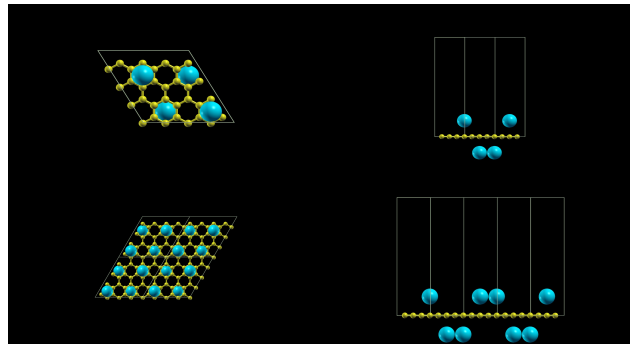


**Figure 19.** In the upper there is the  $K_4C_{32}$  system with  $(4 \times 4)$  cell and in the lower there is the replicated  $K_4C_{32}$  system. The carbon-carbon distance is  $d_{c-c} = 1.4111$ .

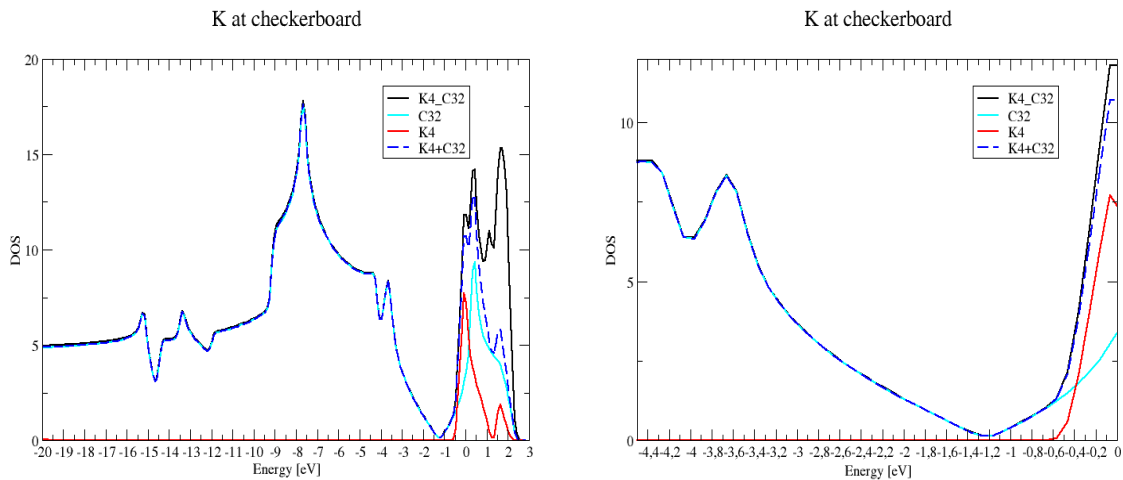


**Figure 20.** The DOS of the  $K_4C_{32}$  system, on the left the full DOS and on the right a range of energy around the Fermi level.

#### 4.6. $C_8KC_8$ with stacking AB

In **Figure 21** the  $C_8KC_8$  with stacking AB system is shown and in **Figure 22** its DOS.

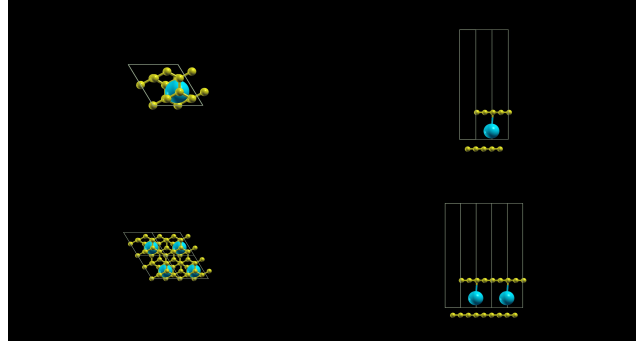


**Figure 21.** In the upper there is the  $C_8KC_8$  system with  $(2 \times 2)$  cell and in the lower there is the replicated  $C_8KC_8$  system. The carbon-carbon distance is  $d_{c-c} = 1.4131$ .

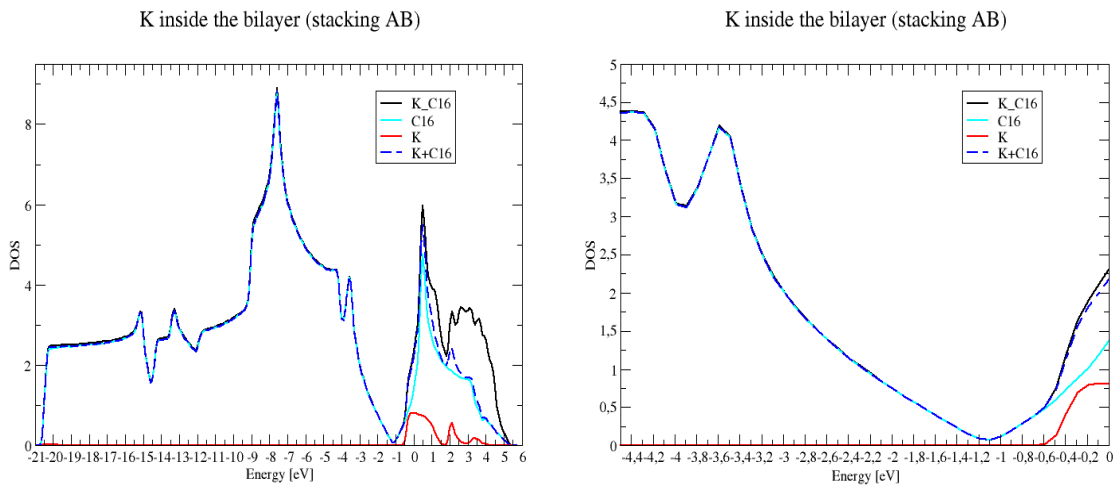


**Figure 22.** The DOS of the  $C_8KC_8$  system, on the left the full DOS and on the right a range of energy around the Fermi level.

#### 4.7. $C_8KC_8$ with stacking AA

In **Figure 23** the  $C_8KC_8$  with stacking AA system is shown and in **Figure 24** its DOS.

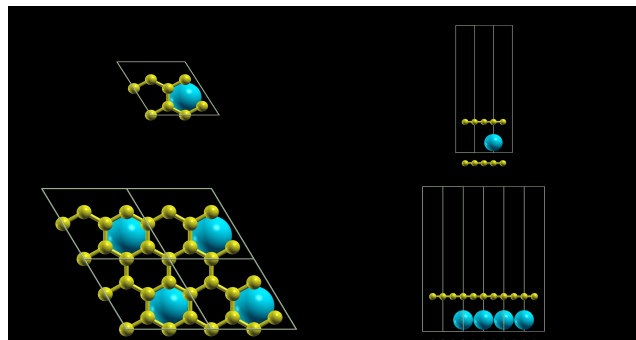


**Figure 23.** In the upper there is the  $C_8KC_8$  system with  $(2 \times 2)$  cell and in the lower there is the replicated  $C_8KC_8$  system. The carbon-carbon distance is  $d_{c-c} = 1.4121$ .

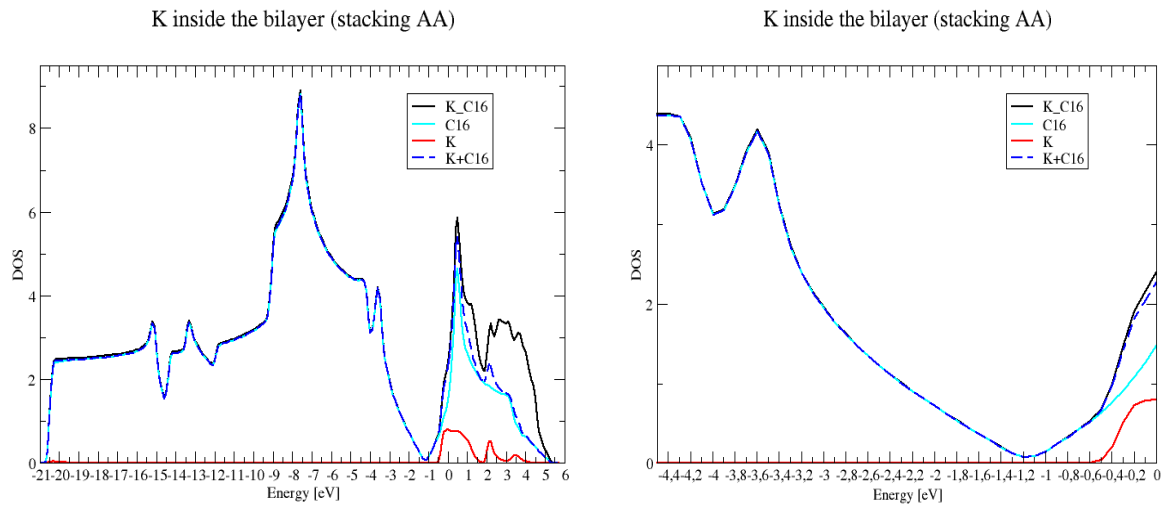


**Figure 24.** The DOS of the  $C_8KC_8$  system, on the left the full DOS and on the right a range of energy around the Fermi level.

#### 4.8. $KC_8C_8$

In **Figure 25** the  $KC_8C_8$  system is shown and in **Figure 26** its DOS.

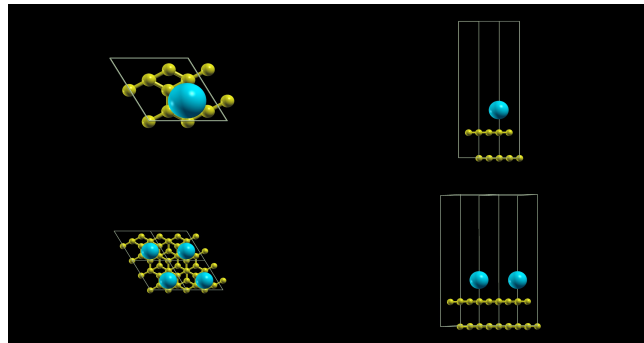


**Figure 25.** In the upper there is the  $KC_8C_8$  system with  $(2 \times 2)$  cell and in the lower there is the replicated  $KC_8C_8$  system. The carbon-carbon distance is  $d_{c-c} = 1.4083$ .

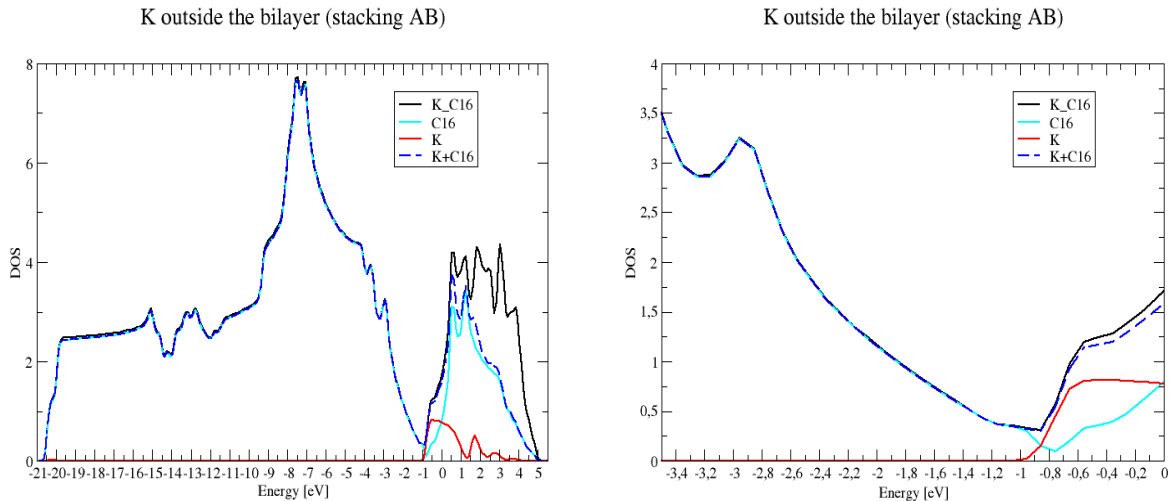


**Figure 26.** The DOS of the  $KC_8C_8$  system, on the left the full DOS and on the right a range of energy around the Fermi level.

### 4.9. $KC_8C_8K$

In **Figure 27** the  $KC_8C_8K$  system is shown and in **Figure 28** its DOS.

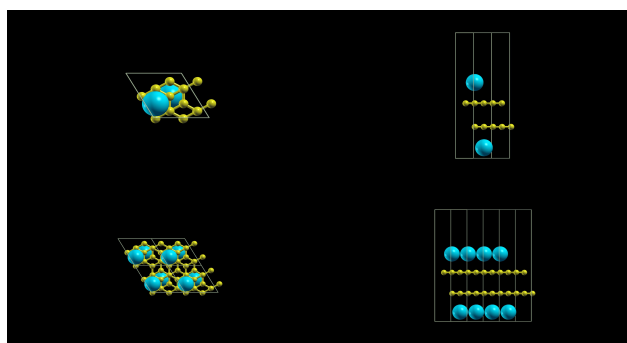


**Figure 27.** In the upper there is the  $KC_8C_8K$  system with  $(2 \times 2)$  cell and in the lower there is the replicated  $KC_8C_8K$  system. The carbon-carbon distance is  $d_{c-c} = 1.4100$ .

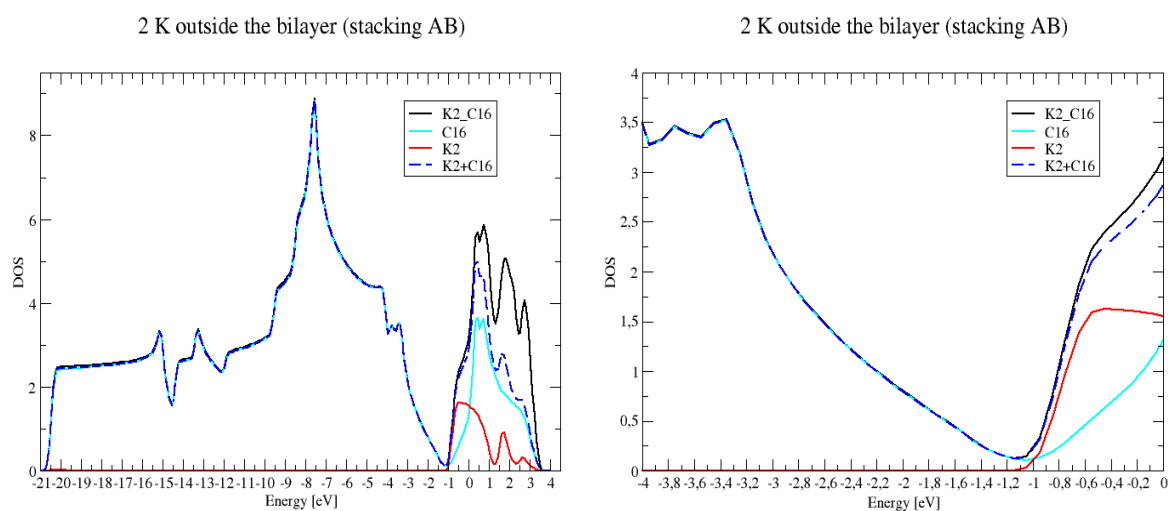


**Figure 28.** The DOS of the  $KC_8C_8K$  system, on the left the full DOS and on the right a range of energy around the Fermi level.

### 4.10. $KC_2$

In **Figure 29** the  $C_8KC_8$  system is shown and in **Figure 30** its DOS.

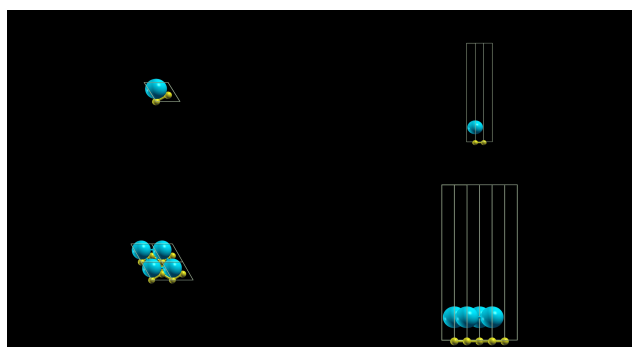


**Figure 29.** In the upper there is the  $KC_2$  system with  $(1 \times 1)$  cell and in the lower there is the replicated  $KC_2$  system. The carbon-carbon distance is  $d_{c-c} = 1.50$ .

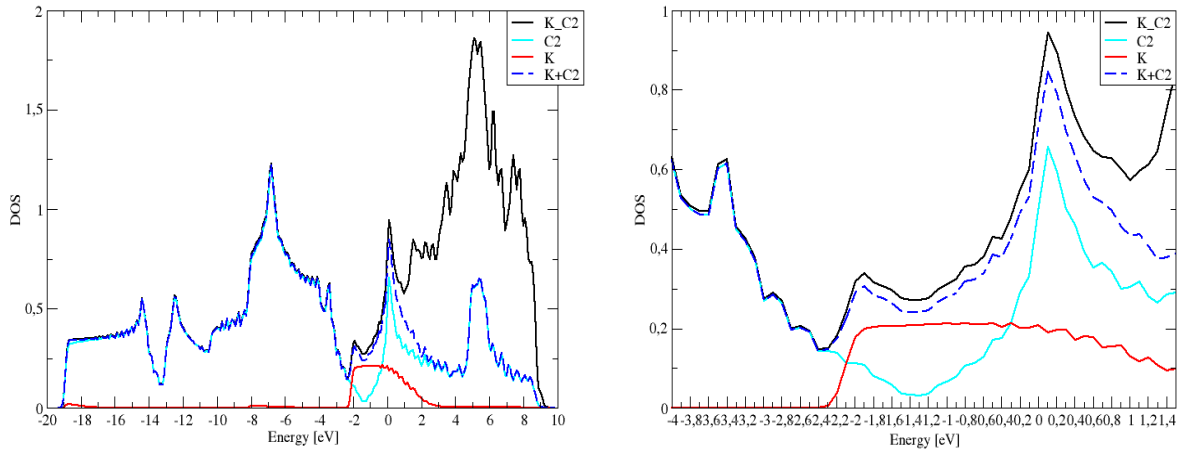


**Figure 30.** The DOS of the  $KC_2$  system, on the left the full DOS and on the right a range of energy around the Fermi level.

#### 4.11. $K_2C_{32}$

In **Figure 31** the  $C_8KC_8$  system is shown and in **Figure 32** its DOS.

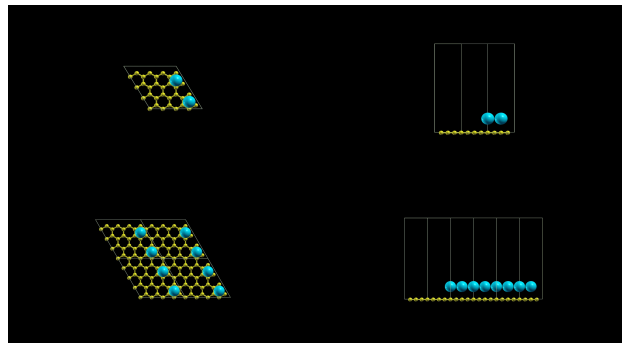


**Figure 31.** In the upper there is the  $KC_{16}$  system with  $(2 \times 2)$  cell and in the lower there is the replicated  $KC_{16}$  system. The carbon-carbon distance is  $d_{c-c} = 1.4106$ .

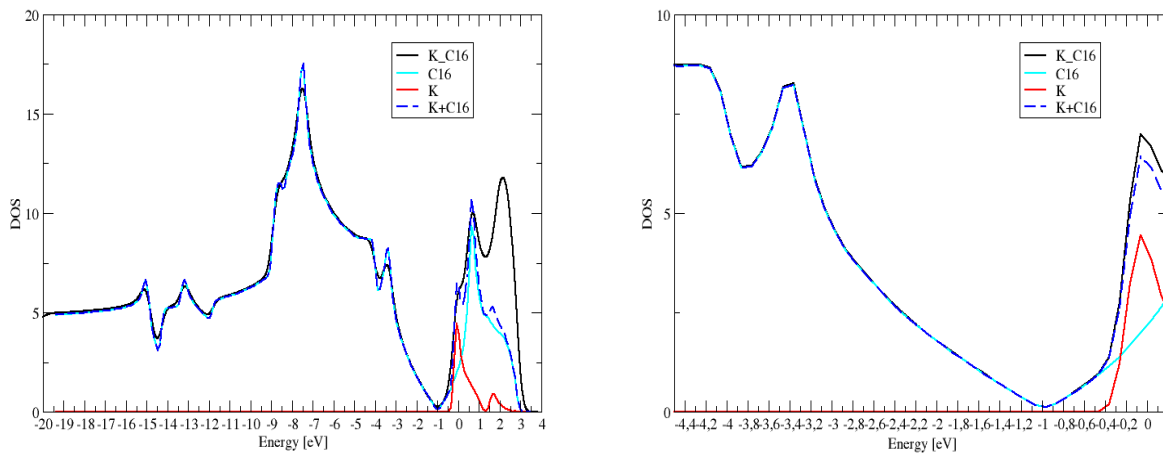


**Figure 32.** The DOS of the  $KC_{16}$  system, on the left the full DOS and on the right a range of energy around the Fermi level.

## 5. Conclusions

Chemical doping is a natural way to increase the performance or personalize the properties of graphene or any other 2D material. The band gap can be produced in graphene by chemical doping with a significant reduction in its carrier mobility [35]. However, there are several methods for modifying the band gap of graphene without the use of traditional chemical doping. These approaches exploit geometry, physical interactions (such as quantum confinement [36] or strain engineering [37]), and structural modifications such as oxidation [38] or the use of multilayer structures [39] to achieve semiconductor-like electronic behavior, opening the band gap of graphene, or simply the application of electric fields [40]. After doping graphene, several mechanisms contribute to the reduction of charge carrier mobility. The main ones are the following: impurity scattering [41], phonon scattering (lattice vibrations) [42], defect [43] and dislocation scattering, local structure distortions. The computational results obtained are well compared to the experimental data of reference [44] shown in **Figure 33** and with some literature dealing with this topic [45–52] and could be useful for predicting material properties [53,54].

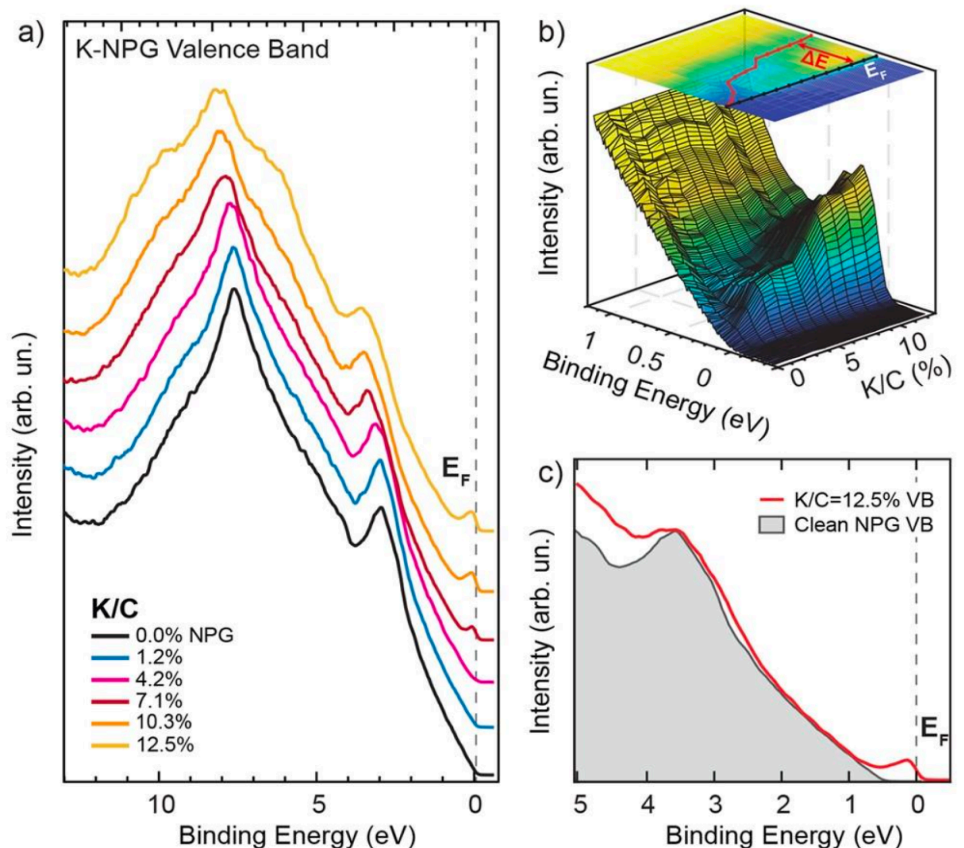


**Figure 33.** (a) UV photoemission spectral density of the K-NPG system as a function of K exposure (spectra vertically stacked for the sake of clarity). (b) Perspective 3D view of the spectral density evolution of the VB close to the Fermi level (black line) as a function of K dose; the Dirac point energy shift  $\Delta E$  due to charge injection is reported as a red line in the top projection of the 3D perspective view. (c) Experimental spectral density of K-NPG at saturation coverage (red line) compared with clean NPG, shifted by  $-0.6$  eV in spectral density (gray filled area) [44].

The experimental results of **Figure 33** are obtained with UPS, ultraviolet photoelectron spectroscopy, ( $\hbar\nu = 21.2$  eV and  $\hbar\nu = 40.8$  eV whose sources are HeI and HeII, respectively) used to probe the surfaces of materials (see **Figure 34**). The most significant observation is an intensity peak at the Fermi energy  $E_F$  in the intercalation compounds. This peak is mainly due to alkali-like  $s$  states [55]. Photoelectron spectroscopy is the most powerful and versatile technique to study the electronic structure of the valence bands in atoms, solids, and molecules (ionization energy of molecules, HOMO).

Multiplying the DOS of the computational calculations with the Fermi-Dirac distribution  $f(E)$ , we get the density of conduction electrons at any particular energy  $N(E) = DOS \cdot f(E)$ . For the Koopmans Theorem we have  $I_i = -\epsilon_i$ , where  $I_i$  is the binding energy of an electron in the state  $i$  and  $\epsilon_i$  is the orbital energy of the state  $i$ -th. Identification of calculated orbital energies with ionization potentials is possible as shown in **Figure 35**.

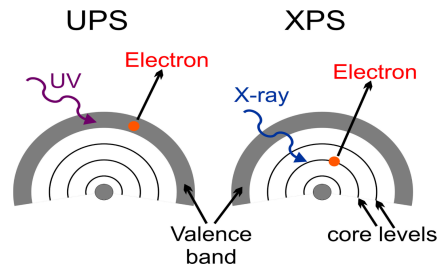


**Figure 34.** With XPS (with  $h\nu > 1000$  eV) the electron emission is a good reflection of the density of states (weighted by the transition rate across the VB). At low photon energies ( $h\nu < 50$  eV) as in UPS the situation is more complex but richer in information.

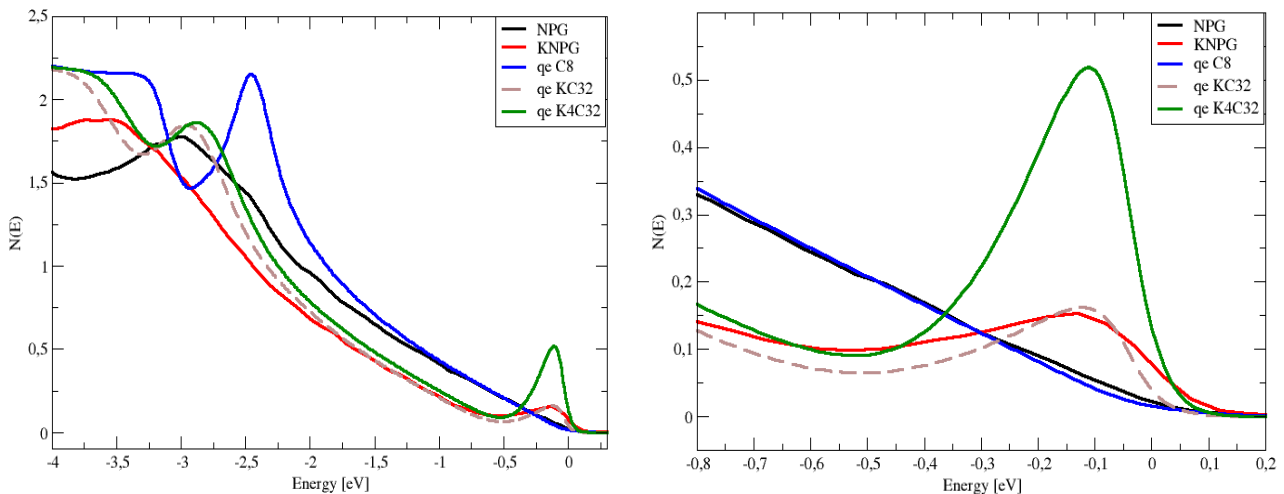


**Figure 35.** Left: Computational results for pristine graphene (QUANTUM ESPRESSO (qe)  $C_8$ ) and K-doped graphene (qe  $K_4C_{32}$  instead of  $KC_8$  and  $KC_{32}$ ) compared with experimental results from reference [44]. Right: A zoom of the same data.

UPS results involving a coverage of 0.3–0.4 ML are very similar to those obtained computationally with QUANTUM ESPRESSO for the  $KC_{32}$  system (1 ML  $\rightarrow KC_8$ ). Finally, it is possible to observe from the total energy values of systems 6,7 and 11 that the bilayer is more favored than the monolayer (it is also possible to verify this for the  $KC_8$  systems) and this compares well with other works [56–58].

The electron donating ability of alkalis, which increases as we move down the group, from Li to Cs [59–66], changes the electronic balance and therefore shifts the Fermi level. Li being the lightest and having a low electronegativity has a tendency to easily donate its valence electron to the graphene surface. Consequently, the introduction of Li is expected to shift the Fermi level upwards, potentially increasing the density of electronic states near the Fermi level. This could increase the conductivity of the system and, in some cases, lead to metallic behavior. Na, although larger than Li maintains a similar behavior, the Fermi level could shift even higher than pure graphene, but to a lesser extent than Li. K being larger than Na tends to donate its valence electron even more easily, but the bond strength between graphene and the adatom is generally weaker. It could be observed that the interaction of potassium with graphene leads to a marked upward shift of the Fermi level but due to the lower electron affinity the effect may be more transient or less stable. Rb and Cs [67], the heavier of the family, the adatoms become even more reactive and tend to donate electrons to graphene more easily. However, the chemical stability of systems with Rb [68] and Cs may decrease, since these alkali atoms tend to have a low adhesion energy to graphene, leading to possible desorption phenomena at relatively low temperatures. In these cases, it could be observed significant shifts of the Fermi level, but with a less stable behavior over time, especially at high temperatures. The interaction between graphene and alkali adatoms, as we have seen, also affects the band structure of the system, in particular the Dirac cone, Li adsorption on graphene may cause minimal distortion of the Dirac cone, but the symmetry of the cone should remain fairly intact. However, a shift in the Fermi level upwards can make the system more conductive. At low concentrations, this effect may not be sufficient to significantly alter the structure of the Dirac cone, but at higher concentrations, changes in the symmetry of the band structure may emerge, with stronger coupling between the graphene electrons and the Li p-orbitals [69]. When Na and K are adsorbed on graphene they can influence the Dirac cone more pronouncedly. The stronger coupling between the alkali s-orbitals and the graphene p-orbitals may lead to more pronounced distortions in the Dirac cone, changing the shape and position of the conduction and valence bands. In particular, the stronger interaction with Na and K may also affect the characteristic symmetry of graphene, leading to asymmetric effects in the cone [70]. For Rb [71] and Cs [72], the interaction with graphene is weaker, but the change in band structure could be significant in terms of the shift and deformation of the Dirac cone. We may see asymmetric deformations in the Dirac cone and a reduction in band structure symmetry, as the heavier alkali adatoms can more strongly influence the local electronic properties of graphene. Li and Na are more stable than their heavier counterparts. Their reactivity may be more easily manageable under experimental conditions, although their adhesion to graphene may not be very strong. This means that the adatom can remain stably adsorbed on graphene, with little problem of desorption at moderate temperatures. K, Rb, and Cs are more reactive and less stable on the graphene surface. These adatoms tend to desorb easily at higher temperatures, and thus the system may not be viable in long-term devices, especially if thermal stability is critical. They could also change the structure of graphene more dramatically, causing structural deformations. Li could be used to improve electronic

conductivity in batteries or other electronic devices. Its high reactivity with graphene could also make it useful for improving energy storage. Na [73] and K are useful for applications where increased conductivity is needed but long-term stability is less critical (e.g., short-lifetime devices or fuel cells). Rb and Cs, due to their low stability on graphene, are not ideal for electronic devices that require stable performance over time. However, they could be explored in transient systems or in basic research.

**Data availability statement:** All data generated or analyzed during this study are included in this published article.

**Institutional review board statement:** Not applicable.

**Informed consent statement:** Not applicable.

**Conflict of interest:** The author declares no conflict of interest.

## References

1. Ahmad S, Miró P, Audiffred M, Heine T. Tuning the electronic structure of graphene through alkali metal and halogen atom intercalation. *Solid State Communications*. 2018; 272: 22–27.
2. Lenchuk O, Adelhelm P, Mollenhauer D. Comparative study of density functionals for the description of lithium-graphite intercalation compounds. *Journal of Computational Chemistry*. 2019; 40(27): 2400–2412.
3. Jishi RA, Guzman DM, Alyahyaei HM. Theoretical investigation of two-dimensional superconductivity in intercalated graphene layers. *Advanced Studies in Theoretical Physics*. 2011; 5(15): 703–716.
4. Dresselhaus MS, Dresselhaus G, Fischer JE. Graphite intercalation compounds: Electronic properties in the dilute limit. *Physical Review B*. 1977; 15(6): 3180.
5. Peralta M, Vaca-Chanatasig C, Vera-Nieto R, Verrilli D. Transport properties of graphene in proximity with alkali metals. *Journal of Physics: Conference Series*. 2022; 2238(1): 012003.
6. Guo B, Fang L, Zhang B, Gong JR. Graphene doping: A review. *Insciences Journal*. 2011; 1: 80–89.
7. Ahmed AB, Said M, Kirfi MM. Dft calculation for adatom adsorption on graphene monolayer using quantum espresso code. *Bayero Journal of Pure and Applied Sciences*. 2022; 13(1): 471–477.
8. Li X, Li J, Ma L, et al.. Graphite anode for potassium ion batteries: Current status and perspective. *Energy & Environmental Materials*. 2022; 5(2): 458–469.
9. Yang J, Yuan Y, Chen G. First-principles study of potassium adsorption and diffusion on graphene. *Molecular Physics*. 2019; 118(1): e1581291.
10. Plunkett GR. Electrical transport measurements show intrinsic doping and hysteresis in graphene pn junction devices [Bachelor's thesis]. Oregon State University; 2017.
11. Yan H. Bilayer graphene: Physics and application outlook in photonics. *Nanophotonics*. 2015; 4(1): 115–127.
12. Sernelius BE. Casimir effects in systems containing 2D layers such as graphene and 2D electron gases. *Journal of Physics: Condensed Matter*. 2015; 27(21): 214017.
13. Fathi D. A review of electronic band structure of graphene and carbon nanotubes using tight binding. *Journal of Nanotechnology*. 2011; 2011: 1–6.
14. Zhang T, Xue Q, Zhang S, and Dong M. Theoretical approaches to graphene and graphene-based materials. *Nano Today*. 2012; 7(3): 180–200.
15. Gusynin VP, Sharapov SG. Transport of Dirac quasiparticles in graphene: Hall and optical conductivities. *Physical Review B*. 2006; 73(24).
16. Oli BD, Bhattarai C, Nepal B, Adhikari NP. First-principles study of adsorption of alkali metals (Li, Na, K) on graphene. In: Giri PK, Goswami DK, Perumal A (editors). *Advanced Nanomaterials and Nanotechnology*. Springer; 2013. pp. 515–529.
17. Antonio H. Neto C. The carbon new age. *Materials Today*. 2010; 13(3): 12–17.
18. Bonzel HP, Bradshaw AM, Ertl G. *Physics and Chemistry of Alkali Metal Adsorption*. Elsevier; 1989.
19. Bennich P, Puglia C, Brühwiler PA, et al. Photoemission study of K on graphite. *Physical Review B*. 1999; 59(12): 8292–8304.

20. Onuma H, Kubota K, Muratsubaki S, et al. Phase evolution of electrochemically potassium intercalated graphite. *Journal of Materials Chemistry A*. 2021; 9(18): 11187–11200.
21. Olsson E, Chai G, Dove M, Cai Q. Adsorption and migration of alkali metals (Li, Na, and K) on pristine and defective graphene surfaces. *Nanoscale*. 2019; 11(12): 5274–5284.
22. Grüneis A, Attaccalite C, Rubio A, et al. Electronic structure and electron-phonon coupling of doped graphene layers in KC8. *Physical Review B*. 2009; 79(20): 205106.
23. Sonia FJ, Jangid MK, Aslam M, et al. Enhanced and faster potassium storage in graphene with respect to graphite: A comparative study with lithium storage. *ACS Nano*. 2019; 13(2): 2190–2204.
24. Ziambaras E, Kleis J, Schröder E, Hyldgaard P. Potassium intercalation in graphite: A van der waals density-functional study. *Physical Review B*. 2007; 76(15): 155425.
25. Caragiu M, Finberg S. Alkali metal adsorption on graphite: A review. *Journal of Physics: Condensed Matter*. 2005; 17(35): R995.
26. Castro Neto AH, Guinea F, Peres NMR, et al. The electronic properties of graphene. *Reviews of Modern Physics*. 2009; 81(1): 109–162.
27. Novoselov KS, Geim AK, Morozov S, et al. Two-dimensional gas of massless dirac fermions in graphene. *Nature*. 2005; 438: 197–200.
28. Wang J, Deng S, Liu Z, Liu Z. The rare two-dimensional materials with dirac cones. *National Science Review*. 2015; 2(1): 22–39.
29. Bandyopadhyay A, Jana D. Dirac materials in a matrix way. *Universal Journal of Materials Science*. 2020; 8(2): 32–44.
30. Wehling TO, Black-Schaffer AM, Balatsky AV. Dirac materials. *Advances in Physics*. 2014; 63(1): 1–76.
31. Yun HJ, Park S. Newly written physics in graphene. *New Physics: Sae Mulli*. 2012; 62(12): 1229.
32. Scandolo S, Giannozzi P, Cavazzoni C, et al. First-principles codes for computational crystallography in the quantum-espresso package. *Zeitschrift für Kristallographie-Crystalline Materials*. 2005; 220(5–6): 574–579.
33. Wei Z, Guo D, Hou Y, et al. Progress on the graphene-involved catalytic hydrogenation reactions. *Journal of the Taiwan Institute of Chemical Engineers*. 2016; 67: 126–139.
34. Chan KT, Neaton JB, Cohen ML. First-principles study of metal adatom adsorption on graphene. *Physical Review B*. 2008; 77(23): 235430.
35. Mir SH, Yadav VK, Singh JK. Recent advances in the carrier mobility of two-dimensional materials: A theoretical perspective. *ACS Omega*. 2020; 5(24): 14203–14211.
36. Zhao J, Ji P, Li Y, et al. Ultrahigh-mobility semiconducting epitaxial graphene on silicon carbide. *Nature*. 2024; 625: 60–65.
37. Yang S, Chen Y, Jiang C. Strain engineering of two-dimensional materials: Methods, properties, and applications. *InfoMat*. 2021; 3(4): 397–420.
38. Lee HY, Haidari MM, Kee EH, et al. Charge Transport in UV-Oxidized Graphene and Its Dependence on the Extent of Oxidation. *Nanomaterials*. 2022; 12(16): 2845.
39. Tahani M, Shohany BG, Motevalizadeh L. Study of structural, electronic, and mechanical properties of pure and hydrogenated multilayer penta-graphene nano-plates using density functional theory. *Materials Today Communications*. 2021; 28: 102608.
40. Silva DHS. Band gap opening in Bernal bilayer graphene under applied electric field calculated by DFT. *Physica B: Condensed Matter*. 2024; 694: 416398.
41. Zhang S, Chuang HJ, Le ST, et al. Control of the Schottky barrier height in monolayer WS<sub>2</sub> FETs using molecular doping. *AIP Advances*. 2022; 12(8).
42. Natarajan V, Naveen Kumar P, Ahmad M, et al. Effect of electron-phonon interaction and valence band edge shift for carrier-type reversal in layered ZnS/rGO nanocomposites. *Journal of Colloid and Interface Science*. 2021; 586: 39–46.
43. Lu X, Guo H, Lei Z, et al. Study of High-Energy Proton Irradiation Effects in Top-Gate Graphene Field-Effect Transistors. *Electronics*. 2023; 12(23): 4837.
44. Marchiani D, Tonelli A, Mariani C, et al. Tuning the electronic response of metallic graphene by potassium doping. *Nano Letters*. 2022; 23(10).
45. Golze D, Dvorak M, Rinke P. The GW Compendium: A Practical Guide to Theoretical Photoemission Spectroscopy. *Frontiers in Chemistry*. 2019; 7: 377.
46. Struzzi C, Praveen CS, Scardamaglia M, et al. Controlled thermodynamics for tunable electron doping of graphene on Ir(111). *Physical Review B*. 2016; 94(8).

47. Lu H, Guo Y, Robertson J. Charge transfer doping of graphene without degrading carrier mobility. *Journal of Applied Physics*. 2017; 121(22).
48. Kihlgrén T, Balasubramanian T, Walldén L, Yakimova R. K/graphite: Uniform energy shifts of graphite valence states. *Surface Science*. 2006; 600(5): 1160–1164.
49. Wang Z, Ratvik AP, Grande T, Sverre M. Diffusion of alkali metals in the first stage graphite intercalation compounds by vdW-DFT calculations. *RSC Advances*. 2015; 5(21): 15985–15992.
50. Bostwick A, Speck F, Seyller T, et al. Observation of Plasmarons in Quasi-Freestanding Doped Graphene. *Science*. 2010; 328(5981): 999–1002.
51. Matsui F, Eguchi R, Nishiyama S, et al. Photoelectron Holographic Atomic Arrangement Imaging of Cleaved Bimetal-intercalated Graphite Superconductor Surface. *Scientific Reports*. 2016; 6(1): 1–10.
52. Preil ME, Fischer JE. X-Ray Photoelectron Study of the Valence Band of KC8: Direct Experimental Proof of Complete K(4s) Charge Transfer. *Physical Review Letters*. 1984; 52(13): 1141–1144.
53. Mir SH, Yadav VK, Singh JK. Recent Advances in the Carrier Mobility of Two-Dimensional Materials: A Theoretical Perspective. *ACS Omega*. 2020; 5(24): 14203–14211.
54. Marzari N, Ferretti A, Wolverson C. Electronic-structure methods for materials design. *Nature Materials*. 2021; 20(6): 736–749.
55. Oelhafen P, Pflüger P, Hauser E, Güntherodt HJ. Evidence for an alkali-like conduction band in alkali graphite intercalation compounds. *Solid State Communications*. 1980; 33(2): 241–244.
56. Sun LF, Dong LM, Wu ZF, Fang C. A comparison of the transport properties of bilayer graphene, monolayer graphene, and two-dimensional electron gas. *Chinese Physics B*. 2013; 22(7): 077201.
57. Shokuhifard R, Fuladvand H. Fundamental differences between mono- and bi-layer graphene. *International Journal of Science and Applied Science Conference Series 3 (Fundamental Differences between Mono- and Bi-layer Graphene)*. 2010; 78–83.
58. Jacak J, Jacak L. Difference in hierarchy of fqhe between monolayer and bilayer graphene. *Physics Letters A*. 2015; 379(36): 2130–2134.
59. Chepkasov IV, Ghorbani-Asl M, Popov ZI, et al. Alkali metals inside bi-layer graphene and mos<sub>2</sub>: Insights from first-principles calculations. *Nano Energy*. 2020; 75: 104927.
60. Ma J, Yang C, Ma X, et al. Improvement of alkali metal ion batteries via interlayer engineering of anodes: from graphite to graphene. *Nanoscale*. 2021; 13(29): 12521–12533.
61. Chepkasov IV, Smet JH, Krasheninnikov AV. Single- and multilayers of alkali metal atoms inside graphene/mos<sub>2</sub> heterostructures: A systematic first-principles study. *The Journal of Physical Chemistry C*. 2022; 126(37): 15558–15564.
62. Wang X, Zhang W, Ni K, et al. Alkali metals induced stacking phase transition of graphite. *Carbon*. 2023; 213: 118295.
63. Zinni J, Camerano L, Speyer L, et al. Charge transfer in alkaline-earth metal graphite intercalation compounds. *Carbon*. 2024; 230: 119652.
64. Zhou J, Lin Z, Ren H, et al. Layered intercalation materials. *Advanced Materials*. 2021; 33(25): 2004557.
65. Zhang Y, Zhang L, Lv T, et al. Two-dimensional transition metal chalcogenides for alkali metal ions storage. *ChemSusChem*. 2020; 13(6): 1114–1154.
66. Vashishth S, Eswaramoorthy M. Investigation of heteroatom doped graphene anode for high-capacity alkali metal-ion batteries. *Electrochemical Society Meeting Abstracts*. 2023; 244(4): 518–518.
67. Lin Y, Matsumoto R, Liu Q, et al. Alkali metal bilayer intercalation in graphene. *Nature communications*. 2024; 15(1): 425.
68. Yadav A, Kobayashi H, Yamamoto T, Nohira T. Electrochemical rubidium storage behavior of graphite in ionic liquid electrolyte. *Electrochemistry*. 2023; 91(1).
69. Wu X, Zheng F, Kang F, Li J. Effects of lithium intercalation in bilayer graphene. *Physical Review B*. 2023; 107(16).
70. Gogina AA, Tarasov AV, Eryzhenkov AV, et al. Adsorption of Na monolayer on graphene covered Pt(111) substrate. *JETP Letters*. 2023; 117(2): 138–146.
71. Lu B, Ru N, Duan J, et al. In-plane porous graphene: A promising anode material with high ion mobility and energy storage for rubidium-ion batteries. *ACS Omega*. 2023; 8(24): 21842–21852.
72. Yadav A, Kobayashi H, Yamamoto T, Nohira T. Electrochemical intercalation of cesium into graphite in ionic liquid electrolyte. *Electrochemistry*. 2024; 92(4).
73. Li S, Dong R, Li Y, et al. Advances in free-standing electrodes for sodium ion batteries. *Materials Today*. 2024; 72: 207–234.